Modeling Ice Shelf Cavities in a z-Coordinate Ocean General Circulation Model

M. Losch

Alfred-Wegener-Institut für Polar- und Meeresforschung, Bremerhaven, Germany

Abstract. Processes at the ice shelf-ocean interface and in particular in ice shelf cavities around Antarctica have an observable effect on the solutions of basin scale to global coupled ice-ocean models. Despite this, these processes are not routinely represented in global ocean and climate models. It is shown that a new ice shelf cavity model for z-coordinate models can reproduce results from an intercomparison project of earlier approaches with vertical σ- or isopycnic coordinates. As a proof of concept, ice shelves are incorporated in a 100 year global integration of a z-coordinate model. In this simulation, glacial melt water can be traced as far as north as 15° S. The observed effects of processes in the ice shelf cavities agree with previous results from a σ-coordinate model, notably the increase in sea ice thickness. However, melt rates are overestimated probably because the parameterization of basal melting does not suit the low resolution of this configuration.

1. Introduction

About 50 % of the Antarctic continental margin is covered by ice shelves [*Fox and Cooper*, 1994]. Ice shelf cavities are found where the continental ice sheets and outlet glaciers reach the ocean and ice masses float, owing to their lower density compared to sea water. Ice shelf thicknesses vary from more than a thousand meters near the grounding line to about two hundred meters near the ice shelf edge. Depending on the location of the ice shelf, warm deep water (e.g., Circumpolar Deep Water at Pine Island Glacier) and/or High Salinity Shelf Water (e.g., Filchner-Ronne Ice Shelf) can enter the cavities. There it melts the ice shelf base, rises with the melt water along the inclined ice shelf base and — in some parts — (re-)freezes due to the pressure dependence of the freezing point of sea water [0.753° K/1000 dBar, *Millero*, 1978], forming Ice Shelf Water (ISW). The circulation associated with these processes is known as the ice pump [*Lewis and Perkins*, 1986]. Basal melt water around Antarctica contributes approximately 28 mSv ($1\,\mathrm{Sv} = 10^6\,\mathrm{m}^3\,\mathrm{s}^{-1}$ and $1\,\mathrm{mSv} = 10^3\,\mathrm{m}^3\,\mathrm{s}^{-1}$) of freshwater to the Southern Ocean [*Hellmer*, 2004]. Weddell Sea Bottom Water forms by mixing between Ice Shelf Water and Weddell Deep Water [*Foldvik et al.*, 1985] so that ice shelf processes contribute to the deep branch of the global ocean circulation. *Hellmer* [2004] claimed that models without ice shelf cavities and the freshwater deficit associated with them tend not only to underestimate sea ice thickness but more importantly to increase the bottom water formation and overturning. Improved estimates of the ocean state from both regional and global ocean models would therefore require inclusion of the effects of ice shelf-ocean interaction [*Hellmer et al.*, 2005; *Thoma et al.*, 2006; *Schodlok et al.*, 2007].

Up to now, models with an explicit treatment of Antarctic ice shelves employ either bottom-following (σ) or isopycnic coordinates [*Beckmann et al.*, 1999; *Timmermann et al.*, 2002a; *Hunter et al.*, 2004; *Holland and Jenkins*, 2001; *Jenkins and Holland*, 2002; *Grosfeld et al.*, 1997; *Gerdes et al.*, 1999; *Thoma et al.*, 2006]. The vertical levels of a σ-coordinate model follow the ice shelves' base and thus provide a convenient way of resolving the ice shelf topography. Ice shelf processes can be included in σ-models with little technical effort: The surface layer is subducted beneath the ice shelf and all ice-ocean interactions are applied to the surface level. However, models using bottom-following coordinates suffer from spurious motion due to the numerical representation of the pressure gradient terms. Therefore, a priori, one expects the resulting errors to be large near the ice shelf edges where σ-coordinates are "bent" from surface values to approximately 200 m depth. For this reason, *Beckmann et al.* [1999] modified the ice shelf edge topography to allow the σ-coordinates to vary smoothly across this discontinuity. In a different approach, *Grosfeld et al.* [1997] introduced hybrid coordinates (z-coordinates near the surface and σ-coordinates beneath the ice shelves) to resolve the steep topography at the ice shelf front.

Isopycnic coordinate models, on the other hand, are a natural choice for density-driven flows in ice shelf cavities (and the ocean in general). However, these models require a non-isopycnic layer to admit (surface or ice-ocean interface) buoyancy forcing. With such a layer, some of the benefits of isopycnic coordinates are lost [*Holland and Jenkins*, 2001]. Further, isopycnic models are traditionally formulated in terms of potential density. Difficulties associated with this choice (in particular the absence of a unique reference point for the potential density) have probably prevented the general use of isopycnic coordinate models in a global context. Newer formulations with hybrid coordinates have overcome these limitations [e.g., HYCOM, *Bleck*, 2002].

To date, many global ocean models are still formulated in z-coordinates, so that previous ice shelf cavity implementations for σ- or isopycnic coordinates cannot be used for these models. For this reason, *Beckmann and Goosse* [2003] proposed a parameterization of ice shelf-ocean interaction based on the experience with high resolution σ-coordinate models [*Beckmann et al.*, 1999; *Timmermann et al.*, 2002a]. In this paper, the first explicit model of ice shelf cavities in a z-coordinate general circulation model is presented. Z-coordinate models are known to have difficulties representing bottom boundary layers and downslope flow due spurious diabatic mixing. *Legg et al.* [2006] found that downslope flow of dense plumes depends strongly on horizontal and vertical resolution: only at intermediate to high horizontal and vertical resolution a z-coordinate model gives results similar to an isopycnic model. Similar difficulties are anticipated for the representation of light plumes rising along the shelf ice topography. On the other hand, z-coordinate models do not not suffer from pressure gradient errors. The partial cell treatment of topography [*Adcroft et al.*, 1997] ensures an accurate representation of topography in the ice shelf cavities.

Section 2 describes the Massachusetts Institute of Technology general circulation model [MITgcm, *MITgcm Group*, 2002] and specifically the modifications necessary to include ice shelf cavities. In Section 3, model performance is compared to the results of ISOMIP (Ice-Shelf Ocean Model Intercomparison Project) test experiments [*Holland et al.*, 2003]. A coarse but realistic global model with ice shelf cavities is presented in Section 4, where the impact of ice shelf cavities on the general circulation is also demonstrated. Conclusions are presented in Section 5.

2. Model Description: Ice Shelf-Water Interaction in a z-Level Model

The M.I.T. General Circulation Model (MITgcm) is a general purpose grid-point algorithm that solves the Boussinesq form of the Navier-Stokes equations for an incompressible fluid, hydrostatic or fully non-hydrostatic, with a spatial finite-volume discretization on a curvilinear computational grid (in the present context on a three-dimensional longitude, latitude, depth grid). The model algorithm is described in *Marshall et al.* [1997]; for online documentation and access to the model code, see *MITgcm Group* [2002].

2.1. Dynamics

The dynamical core of the MITgcm has been used in z-coordinate modeling of the ocean circulation and pressure coordinate modeling of the atmosphere [*Marshall et al.*, 2004]. *Losch et al.* [2004] used the same concept as *Marshall et al.* for constructing an ocean model in pressure coordinates. In this configuration, the free surface, which is at the top of the water column in z-coordinates, is interpreted as bottom pressure (anomaly) along the castellated bottom topography or surface orography. The shelf ice topography on top of the water column has a similar role as (and in the language of *Marshall et al.* [2004] is "isomorphic" to) the orography and the pressure boundary conditions at the bottom of the fluid for atmospheric and oceanic models in pressure coordinates. For this reason, the code infrastructure of the MITgcm requires only very little change for the inclusion of ice shelf topography. The following details of the MITgcm are relevant to implementing an ice shelf cavity model: treatment of hydrostatic (and non-hydrostatic) pressure in conjunction with a linear or a non-linear free surface and partial cells for representing topography accurately.

The total pressure p_{tot} in the ocean can be divided into the pressure at the top of the water column p_{top}, the hydrostatic pressure and the non-hydrostatic pressure contribution p_{NH}:

$$p_{tot} = p_{top} + \int_z^{\eta-h} g\,\rho\,dz + p_{NH}, \qquad (1)$$

with the gravitational acceleration g, the density ρ, the vertical coordinate z (positive upwards), and the dynamic sea-surface height η. For the open ocean, $p_{top} = p_a$ (atmospheric pressure) and $h = 0$. Underneath an ice-shelf that is assumed to be floating in isostatic equilibrium, p_{top} at the top of the water column is the atmospheric pressure p_a plus the weight of the ice-shelf. It is this weight of the ice-shelf that has to be provided as a boundary condition at the top of the water column. The weight is conveniently computed by integrating a density profile ρ^*, that is constant in time and corresponds to the sea-water replaced by ice, from $z = 0$ to a "reference" ice-shelf draft at $z = -h$ [*Beckmann et al.*, 1999], so that

$$p_{top} = p_a + \int_{-h}^0 g\,\rho^*\,dz. \qquad (2)$$

Underneath the ice shelf, the "sea-surface height" η is the deviation from the "reference" ice-shelf draft h. During a model integration, η adjusts so that the isostatic equilibrium is maintained for sufficiently slow and large scale motion.

In the MITgcm, the total pressure anomaly p'_{tot} which is used for pressure gradient computations is defined by substracting a purely depth dependent contribution $-g\rho_0 z$ with a constant reference density ρ_0 from p_{tot}. Eq. (1) becomes

$$p_{tot} = p_{top} - g\,\rho_0\,(z+h) + g\,\rho_0\,\eta + \int_z^{\eta-h} g\,(\rho - \rho_0)\,dz + p_{NH}, \qquad (3)$$

and after rearranging

$$p'_{tot} = p'_{top} \qquad + g\,\rho_0\,\eta + \int_z^{\eta-h} g\,(\rho - \rho_0)\,dz + p_{NH}, \qquad (4)$$

with $p'_{tot} = p_{tot} + g\,\rho_0\,z$ and $p'_{top} = p_{top} - g\,\rho_0\,h$. The non-hydrostatic pressure contribution p_{NH} is neglected in the following.

In practice, the ice shelf contribution to p_{top} is computed by integrating Eq. (2) from $z = 0$ to the bottom of the last fully dry cell within the ice shelf:

$$p_{top} = g \sum_{k'=1}^{n-1} \rho^*_{k'} \Delta z_{k'} + p_a \qquad (5)$$

where n is the vertical index of the first (at least partially) "wet" cell and $\Delta z_{k'}$ is the thickness of the k'-th layer (counting downwards). The pressure anomaly for evaluating the pressure gradient is computed in the center of the "wet" cell k as

$$p'_k = p'_{top} + g\rho_n\eta + g \sum_{k'=n}^k \left((\rho_{k'} - \rho_0)\Delta z_{k'} \frac{1 + H(k'-k)}{2} \right) \qquad (6)$$

where $H(k'-k) = 1$ for $k' < k$ and 0 otherwise.

The partial cell method addresses a severe limitation of z-coordinate models. Without partial cells, the "staircase" representation of topography in such models becomes only reasonable at very high resolution. With partial cells, topography (of the sea floor) can be approximated more accurately than with full cells and this leads to generally smoother solutions that compare favorably with solutions of a terrain-following model [*Adcroft et al.*, 1997].

The application of partial cells for representing topography and fluxes along topography of an ice shelf is completely analogous to that of bottom topography as reported in *Adcroft et al.* [1997]. Grid
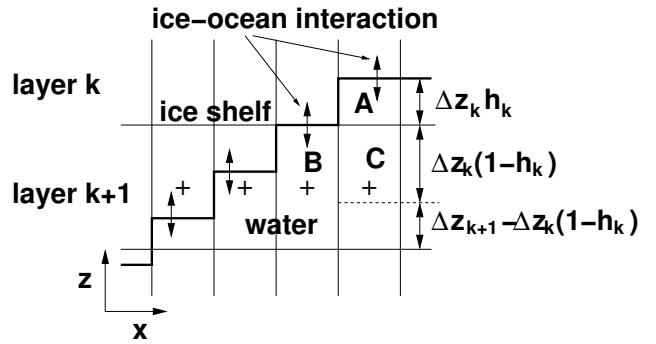

Figure 1. Schematic of a vertical section of the grid at the base of an ice shelf. Grid lines are thin, the thick line is the model's representation of the ice shelf-water interface. Plus-signs mark the position of pressure points for pressure gradient computations. The letters A, B, and C, mark specific grid cells for reference in the text. $h_{i,j,k}$ is the fractional cell thickness, so that $h_{i,j,k}\Delta z_k$ is the actual cell thickness, horizontal indices (i,j) are dropped in the schematic.

Table 1. Model mixing and friction parameters, GM = *Gent and McWilliams* [1990], Leith=*Leith* [1996], KPP = *Large et al.* [1994]

parameter name	ISOMIP 1	global (Section 4)
viscosities and diffusivities		
vertical viscosity	$0.001\,\mathrm{m^2s^{-1}}$	KPP
vertical diffusivity	$0.00005\,\mathrm{m^2s^{-1}}$	KPP
horizontal viscosity	$600\,\mathrm{m^2s^{-1}}$	Leith
horizontal diffusivity	$100\,\mathrm{m^2s^{-1}}$	GM ($\leq 600\,\mathrm{m^2s^{-1}}$)
quadratic stress coefficients		
ice-ocean stress	$0.0025\,\mathrm{m^{-1}}$	$0.0\,\mathrm{m^{-1}}$
bottom stress	$0.0025\,\mathrm{m^{-1}}$	$0.0\,\mathrm{m^{-1}}$

a) barotropic stream function [Sv]

b) overturning stream function [Sv]
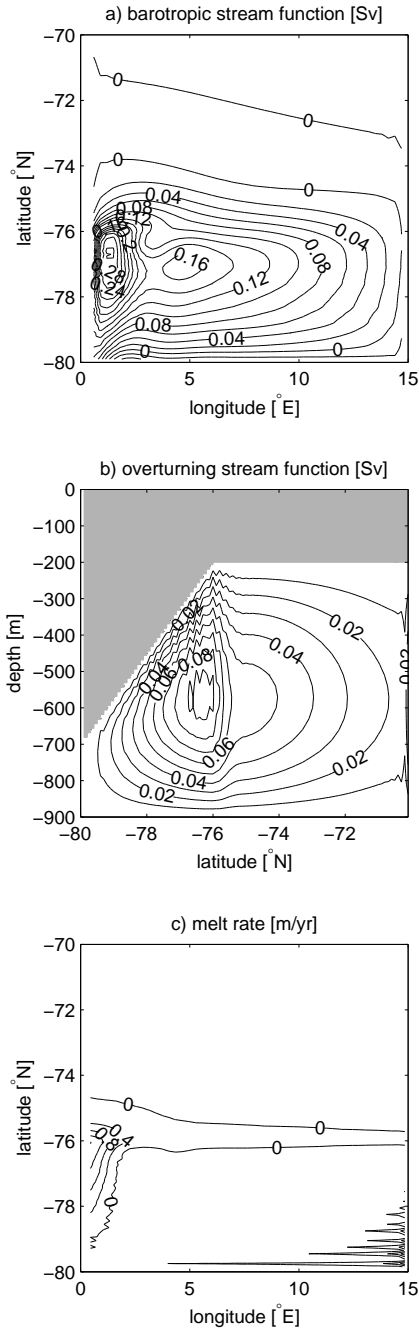
c) melt rate [m/yr]

Figure 2. Steady state solution ISOMIP Experiment 1. Top: Stream function of the vertically integrated mass transport (in Sv); middle: (Overturning) Stream function for the zonally integrated mass transport (in Sv); bottom: Freshwater flux (in m/y) with contour interval 0.4 m/y. The freshwater flux in the southwest corner is negative (melting) and contour labels are omitted for better visibility. Maximum and minimum freshwater fluxes are $1.62\,\mathrm{m/y}$ (freezing) and $-1.56\,\mathrm{m/y}$ (melting), with a mean of $-0.054\,\mathrm{m/y}$ under the inclined ice shelf base.

a) barotropic stream function [Sv]

b) overturning stream function [Sv]

c) melt rate [m/yr]

Figure 3. Same as Figure 2, but with the simple boundary layer scheme. The solution is more energetic in the spin-up phase, because the enhanced mixing allows more water to be cooled by the ice shelf. The noise, in particular in the freshwater flux, is reduced. Maximum/minimum/mean of freshwater flux are $1.77/-2.42/-0.054\,\mathrm{m/y}$.

cells above the base of the ice shelf topography h are "dry" in the same sense as cells below the sea floor. The ice shelf base topography can be approximated more accurately by allowing cells that are partially filled from the bottom; cell A in Figure 1 is an example. In this case, the pressure for evaluating horizontal pressure gradients is still computed for the center (scalar) point (plus signs in Figure 1) of the f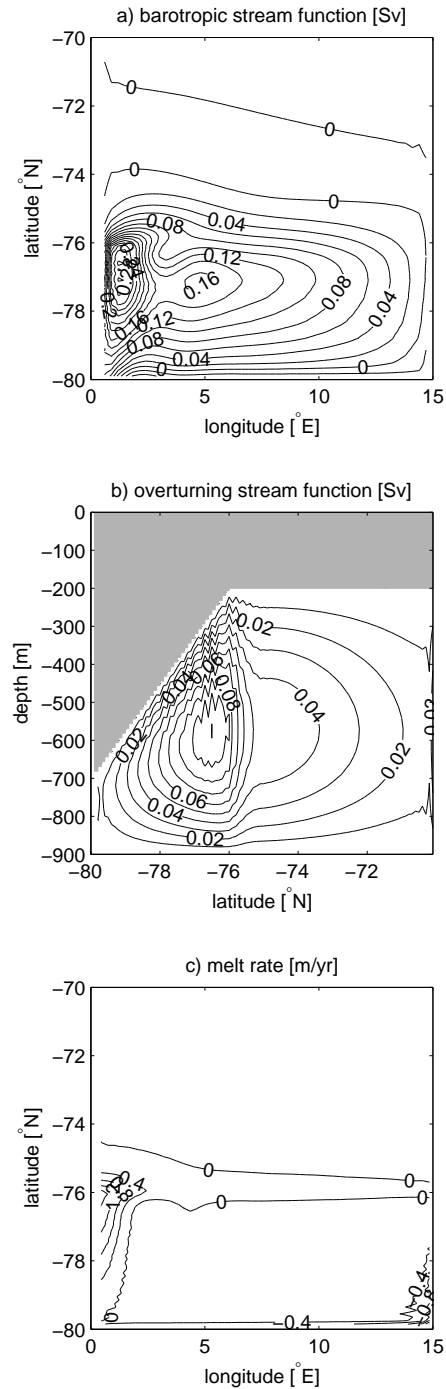ull cell according to Eq. (6) [in the same way as for bottom topography, see *Adcroft et al.*, 1997], even if the cell center lies in the dry part of the cell. With this formulation non-zero pressure gradients in the absence of horizontal density gradients are avoided in a way that is standard for the partial cell method.

2.2. Thermodynamics

Freezing and melting form a boundary layer between ice shelf and ocean which is parameterized following *Grosfeld et al.* [1997] or *Hellmer and Olbers* [1989]. Both parameterizations yield an effective heat flux and a virtual salt flux (i.e., a freshwater flux without volume change in the ocean) between ice shelf and water, that can be conveniently applied at the base of the ice shelf, that is, as a tendency term in the ocean at the appropriate depth. The simpler parameterization similar to *Grosfeld et al.* [1997] is required for the ISOMIP experiments. The more realistic parameterization of *Hellmer and Olbers* [1989] takes into account the dependence of the freezing point of seawater on salinity and generally leads to smaller melt rates than the former. In the present implementation, the conservative formulation of *Jenkins et al.* [2001] is used. Both schemes are outlined in the appendix.

3. ISOMIP experiments

The Ice Shelf–Ocean Model Intercomparison Project (ISOMIP) is an international effort to identify systematic errors in sub-ice shelf cavity ocean models (see http://fish.cims.nyu.edu/project_oisi/isomip/overview.html and *Hunter* [2006] for details). Currently, only data for the "Experiment 1" of "Phase I" are available for comparison. Specifications for an "Experiment 2" are also available. Based on the description of the experiment a rectangular domain with four closed boundaries on the sphere is set up with a horizontal resolution of $0.3°$ in longitude and $0.1°$ in latitude covering a region from $0°$ E to $15°$ E and $80°$ S to $70°$ S; hence, the horizontal grid spacing ranges from approximately 6 to 11 km. 30 layers of thickness 30 m cover the depth of 900 m. The ice-shelf base is at 200 m depth north of $76°$ S and increases linearly to 700 m depth towards the southern boundary so that the entire domain is covered with an ice shelf. The bottom is flat at 900 m depth [see also *Grosfeld et al.*, 1997]. Mixing and friction parameters are given in Table 1.

Density is computed by a nonlinear equation of state [*Jackett and McDougall*, 1995]. The pressure dependence of density is approximated by a depth dependence ($p(z) \approx -g\rho_0 z$). While this (very common) approximation can lead to errors of up to 3 Sv in GCMs [*Dewar et al.*, 1998], it simplifies specifying the initial pressure at the base of the ice shelf. For the realistic simulations in Section 4 this approximation is replaced by an exact treatment of pressure [*Losch et al.*, 2004]. In the case of unstable conditions, vertical convection is parameterized by a simple convective adjustment scheme. Other schemes are available [e.g., the so-called implicit diffusion, and KPP, *Large et al.*, 1994] but do not alter the present results significantly.

For comparison with other ISOMIP experiments and *Grosfeld et al.* [1997] the horizontal stream function, the meridional overturning stream function and basal melt rates are shown at day 10,000 (27.8 years) of the integration when the system is in quasi-steady state.

3.1. Experiment 1

The water is initially at rest and has uniform potential temperature ($-1.9\,°$C) and salinity (34.4). As described by *Grosfeld et al.* [1997] the thermodynamic processes along the sloping ice-water interface cause cold but fresh water to rise along the ice shelf base thereby stretching the water column. This vorticity forcing drives a gyre with a western boundary current of 0.31 Sv underneath the sloping ice shelf base and a meridional overturning of 0.095 Sv (Figure 2). Both shape and magnitude of the circulation are comparable to ISOMIP results which are available at http://fish.cims.nyu.edu/project_oisi/isomip/experiments/phase_I/overview.html. The z-coordinate solution agrees with the solutions of the σ- and isopycnic models where the western boundary current transport ranges from 0.3 to 0.36 Sv and the overturning from 0.08 to 0.09 Sv.

The magnitude of melt rates is also comparable to other ISOMIP results. There is melting of approximately 1 m/y in the south-east corner of the domain, where warm water from the interior is brought
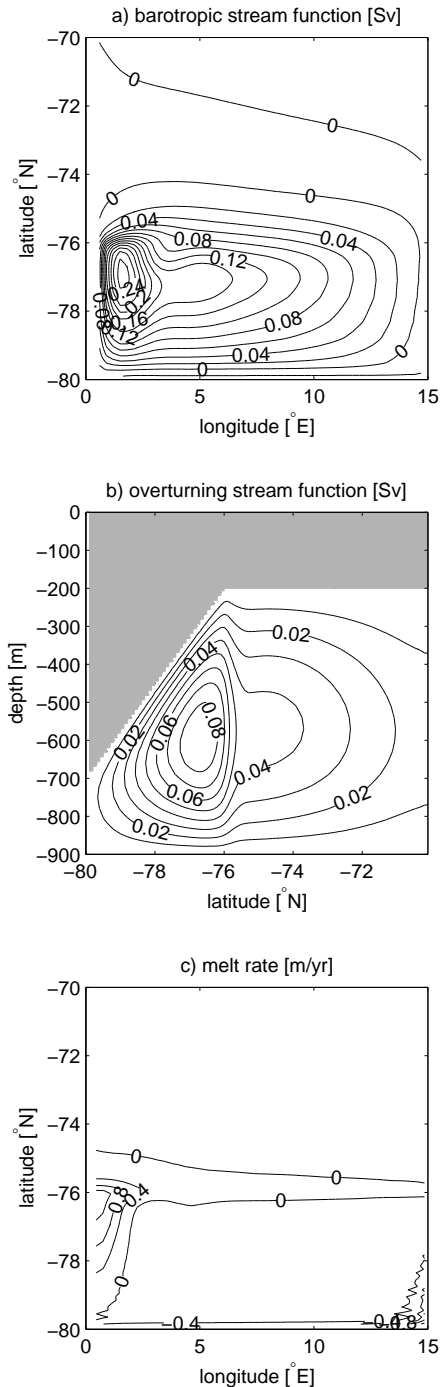

Figure 4. Same as Figure 2, but with the C-D grid and boundary layer scheme. The noise in the stream functions has disappeared. Maximum/minimum/mean of freshwater flux are $1.41/-1.74/-0.048$ m/y.

into contact with the ice shelf, and freezing of approximately 1 m/y along the western boundary current, where cold water rises and refreezes because of the pressure-dependent freezing point of seawater.

There is a striking difference between the previous ISOMIP solutions and the results of the present z-coordinate model. The z-coordinate solution is very noisy in space, which can be seen particularly in the melt rates and to a lesser extent in the overturning stream function. The noise in the melt rates is clearly aligned with individual grid cells and can be explained as follows: The partial

cell treatment of the ice shelf topography results in adjacent cells with decreasing thicknesses within one layer (see the schematic in Figure 1). The heat flux, or equivalently the melt rate (Eq. (A3) in the appendix), is proportional to the difference between the temperature in ocean and at the ice shelf base $T_W - T_b$, but the resulting temperature tendency is proportional to the heat flux per grid-cell volume, so that larger (thicker) cells are cooled more slowly than smaller (thinner) cells. Hence, for a T_b fixed at the freezing point, $T_W - T_b$ remains larger in thicker cells and this leads to larger heat fluxes (or melt rates) at the ice-water interface. Thus, following the ice shelf topography downwards, one encounters decreasing cell thicknesses (decreasing temperatures and heat fluxes) until a layer is crossed where the cell thickness jumps from thin to thick (small heat flux to large heat flux, e.g. cell A and B in Figure 1). This jump is present at each instance in which the topography intersects a layer leading to repeated local maxima in heat flux and hence noise.

In a σ-model, the thickness of the layer along the ice shelf base varies slowly (and more importantly monotonically in the ISOMIP configuration) so that "noise" due to jumps in layer thickness can not develop. In principle, vertical water mass exchange between grid cells should reduce this problem in z-coordinate models, but in practice this vertical exchange is too slow.

Introducing a simple boundary layer reduces the noise problem at the cost of increased vertical mixing. For this purpose the water temperature at the k-th layer abutting ice shelf topography (e.g., cell A in Figure 1) for use in the heat flux parameterizations is computed as a mean temperature $\overline{\theta}_k$ over a boundary layer of the same thickness as the layer thickness Δz_k:

$$\overline{\theta}_k = \theta_k h_k + \theta_{k+1}(1 - h_k) \qquad (7)$$

where $h_k \in (0, 1]$ is the fractional layer thickness of the k-th layer. The original contributions due to ice shelf-ocean interaction g_θ to the total tendency terms G_θ in the time-stepping equation $\theta^{n+1} = f(\theta^n, \Delta t, G_\theta^n)$ are

$$g_{\theta,k} = \frac{Q}{\rho_0 c_p h_k \Delta z_k} \text{ and } g_{\theta,k+1} = 0 \qquad (8)$$

for layers k and $k + 1$ (c_p is the heat capacity). Averaging these terms over a layer thickness Δz_k (e.g., extending from the ice shelf base down to the dashed line in cell C) and applying the averaged tendency to cell A (in layer k) and to the appropriate fraction of cells C (in layer $k + 1$) yields

$$g_{\theta,k}^* = \frac{Q}{\rho_0 c_p \Delta z_k} \qquad (9)$$

$$g_{\theta,k+1}^* = \frac{Q}{\rho_0 c_p \Delta z_k} \frac{\Delta z_k (1 - h_k)}{\Delta z_{k+1}}. \qquad (10)$$

Eq. (10) describes averaging over the part of the grid cell $k + 1$ that is part of the boundary layer with tendency $g_{\theta,k}^*$ and the part with no tendency. Salinity is treated in the same way. The momentum equations are not modified.

Figure 3 shows the effect of the boundary layer scheme. Through averaging, the scheme increases the vertical diffusion near the ice-water interface so that more warm water reaches the interface and melting increases. As a result, the ocean is cooler and fresher than without the boundary layer scheme. Further, the circulation is stronger in the spin-up phase (not shown), but is very similar to the original circulation in steady state. The noise in the buoyancy flux fields is reduced.

The noise in the velocity fields (stream functions) is typical for C-grid models that do not resolve the Rossby radius. The necessary averaging of the Coriolis term on a C-grid leads to a dispersion relation of waves with false minima and hence incorrect group velocities for some short waves. When grid scale energy is generated, for example near topography, grid scale waves can feed energy into short-scale perturbations thus allowing standing grid scale noise to persist [e.g., *Adcroft et al.*, 1999]. *Adcroft et al.* [1999] suggested a coupled C-D grid, where horizontal velocities are evaluated on both
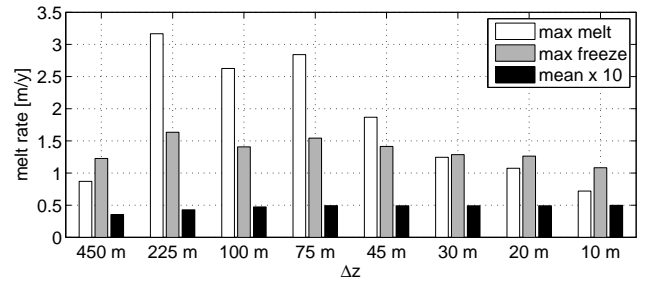

Figure 5. Mean, minimum (maximal freezing), and maximum melt rate (in m/y) as a function of vertical resolution. Mean melt rates are scaled by a factor of ten and refer to the mean under the inclined ice shelf base. $\Delta z = 30\,\mathrm{m}$ corresponds to the solution in Figure 4.

a C-grid and a D-grid to avoid averaging for the evaluation of the Coriolis term. This algorithm is implemented in the MITgcm and the computational modes are damped by relaxing the D-grid velocities to the C-grid velocities with a relaxation time scale of 400,000 seconds. With these parameters, the noise in the stream functions disappears completely (Figure 4) at the cost of additional dissipation which reduces the maxima of the horizontal and overturning stream functions to 0.27 Sv and 0.089 Sv, respectively. Instead of the C-D scheme, bi-harmonic viscosity may be used to damp the noise effectively (not shown).

In order to understand the noise in the overturning stream function, consider a region where the ice shelf topography intersects a grid layer (Figure 1). Cells A and B are subject to melting and freezing at the ice-water interface, whereas cell C is not. Therefore, a density difference is maintained between cells B and C that drives a geostrophic current along the ice shelf base. This mechanism is only present where the ice shelf topography cuts through grid layers and thus lead to singular velocities and thus noise. The horizontal jumps in density are also present in a experiment with large vertical cell thicknesses and not using partially-filled cells, where the noise problem, in agreement with *Adcroft et al.* [1997], is much larger (not shown).

In summary, both cooling as a function of cell thickness and the excitation of grid scale waves, produce noise patterns that are stationary, but that do not jeopardize the numerical stability of the solution, and can be addressed with the above methods.

3.2. Effects of horizontal mixing and vertical resolution

The ISOMIP values for horizontal mixing lead to rather viscous solutions. In a z-coordinate model, mixing is strictly horizontal [in the absence of an eddy mixing scheme as in *Gent and McWilliams*, 1990], and strong mixing coefficients emphasize this effect. Figure 6 illustrates this bias along with a standard solution. With the standard horizontal mixing coefficient for ISOMIP (left panel of Figure 6) the light plume rises along the ice shelf base, but is diluted laterally by horizontal mixing. Without explicit diffusion ($\kappa_h = 0\,\mathrm{m^2 s^{-1}}$) and reduced numerical diffusion (with the help of a high-order advection scheme following *Daru and Tenaud* [2004], A. Adcroft, pers. comm.) the plume is much thinner (center). Isopycnic mixing according to *Gent and McWilliams* [1990], but without the skew flux, makes the plume slightly thicker, but compared to the horizontal mixing case, the lateral dilution of the plume is much reduced (right panel). With the current grid resolution, both slope and plume are resolved. However, if the vertical and horizontal resolution is not sufficient to resolve the topographic slope—as is typically the case in overflow regions in global ocean models—z-coordinate models have difficulties representing flow along such a slope [*Legg et al.*, 2006].

In order to assess the impact of vertical resolution, the experiment is repeated for layer thicknesses of 450 m (2 layers), 225 m
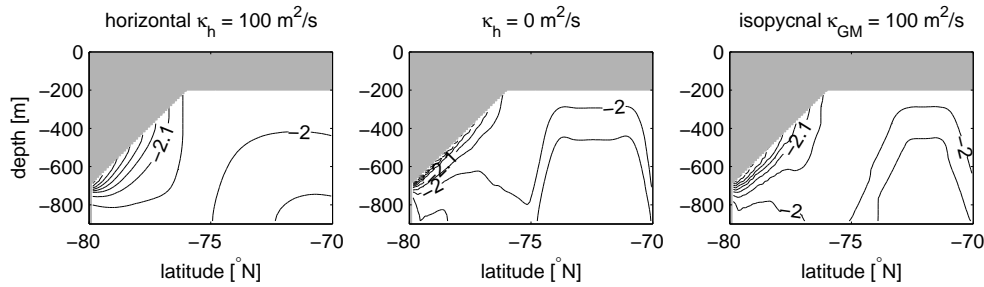
Figure 6. Meridional temperature section in the center of the domain along 7.5° E for the standard experiment with strong horizontal mixing (left, $\kappa_h = 100\,\mathrm{m^2 s^{-1}}$), without explicit horizontal diffusivity (center, $\kappa_h = 0$), and with isopycnal mixing (right, $\kappa_h = 0$ and $\kappa_{GM} = 100\,\mathrm{m^2 s^{-1}}$).
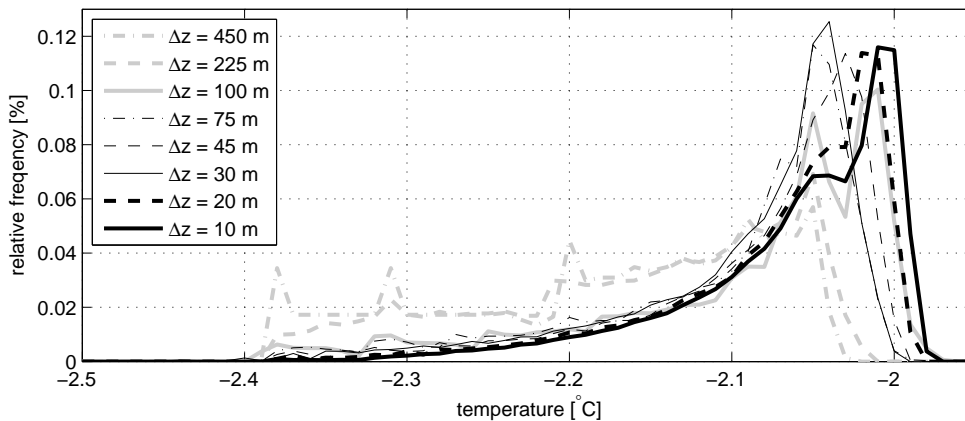

Figure 7. Histogram of temperatures as a function of vertical resolution. $\Delta z = 30\,\mathrm{m}$ corresponds to the solution in Figure 4.

(4 layers), 100 m (9 layers), 75 m (12 layers), 45 m (20 layers), 30 m (30 layers, this is the standard case), 20 m (45 layers), and 10 m (90 layers). Figure 5 shows the mean, minimum, and maximum melt rates as a function of layer thickness. Note that, because of the closed domain, the total heat and freshwater flux between ice and ocean is required to be zero in steady state; the mean melt rates in Figure 5 refer to the mean beneath the inclined ice-shelf base, because only this quantity can be affected by the resolution in this experiment. Mean melt rates are slightly lower for very low resolution, but remain nearly constant for $\Delta z \leq 100\,\mathrm{m}$. Maximum freezing rates become smaller with very high vertical resolution. Maximum melt rates reduce with smaller Δz; these maximum melt rates are found in thick cells next to very thin cells (at topography-layer intersections), in agreement with the discussion of the noise in Figure 2. Figure 7 gives an impression of mixing and dilution by means of a histogram of temperature values normalized by the total number of grid points. For vertical layer thicknesses $\leq 100\,\mathrm{m}$, the temperature distribution is stable along the ice shelf base (low temperatures). Smaller layer thicknesses allow warmer temperatures near the bottom of the interior because of a sharper pycnocline underneath the ice shelf and reduced vertical mixing. At least in this configuration with this particular slope and horizontal resolution, $\Delta z = 100\,\mathrm{m}$ appears to be the minimum vertical resolution that is required to resolve ice shelf-ocean processes.

4. Global Ocean Circulation Model with Ice Shelf Cavities

The advantage of an ice shelf cavity model in z-coordinates is its straightforward applicability to existing global ocean models with z-coordinates. Up to now, the majority of global models are z-coordinate models and adding an ice shelf cavity model in, say, σ-coordinates to such a model requires considerable recoding. In this section results from a comparison of a "standard", but coarse ocean general circulation model in z-coordinates with and without explicit modeling of ice shelf cavities are presented.

4.1. Model configuration

A (nearly) global ocean model (excluding the Arctic Ocean) with sea ice is set up at a nominal resolution of $2°$. In the northern hemisphere the grid spacing is constant at $2°$ and the domain is closed at $80°$ N in order to avoid any difficulties associated with the convergence of latitudes and the pole singularity. In the southern hemisphere, the grid spacing is locally isotropic, that is, the latitude (ϕ) spacing is scaled by $\cos\phi$, giving a resolution of 100 km near $60°$ S and around 50 km in the ice shelf regions of the Ross Sea and the Filchner-Ronne Ice Shelf in the Weddell Sea. While 23 vertical layers allow only limited vertical resolution in the ice shelf cavities, this situation represents a typical problem of z-coordinate models: the vertical resolution near the bottom is poor. This problem is partially alleviated by the partial cell treatment of topography [*Adcroft et al.*, 1997]. The layer thicknesses are 10, 10, 15, 20, 20, 25, 35, 50, 75, 100, 150, 200, 275, 350, 415, 450, and $7 \times 500\,\mathrm{m}$.

Realistic topography is derived from a combination of GEBCO [*British Oceanographic Data Center*, 2003] and the Smith and Sandwell topography [*Smith and Sandwell*, 1997; *Marks and Smith*, 2006]; the ice shelf topography is taken from the Bremerhaven Regional Ice Ocean System [BRIOS, *Beckmann et al.*, 1999] and interpolated to the computational grid. Because of the coarse resolution, no attempt to resolve the small Antarctic ice shelves has been made; only the large ice shelf in the Ross Sea and the Filchner-Ronne Ice Shelf in the Weddell Sea are considered here.

The ocean model is initialized with temperature and salinity climatology [*Levitus et al.*, 1994; *Levitus and Boyer*, 1994] and forced by daily wind, air temperature and humidity, downward long and short wave radiation fields, monthly precipitation fields and a constant run-off field. All fields are part of the climatology ("normal
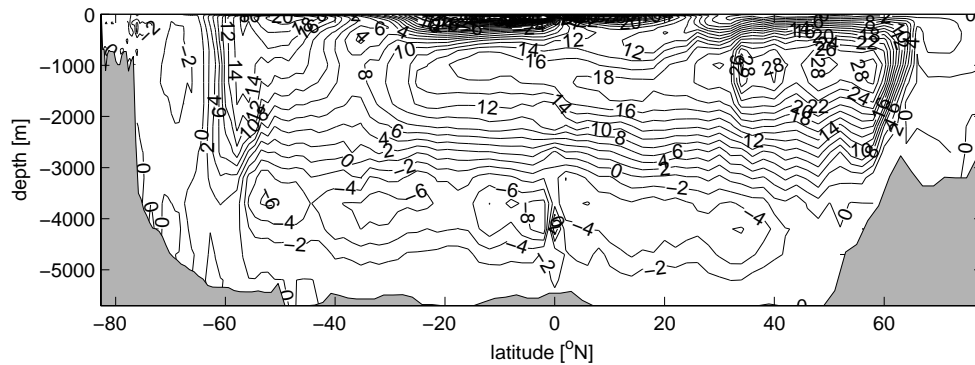
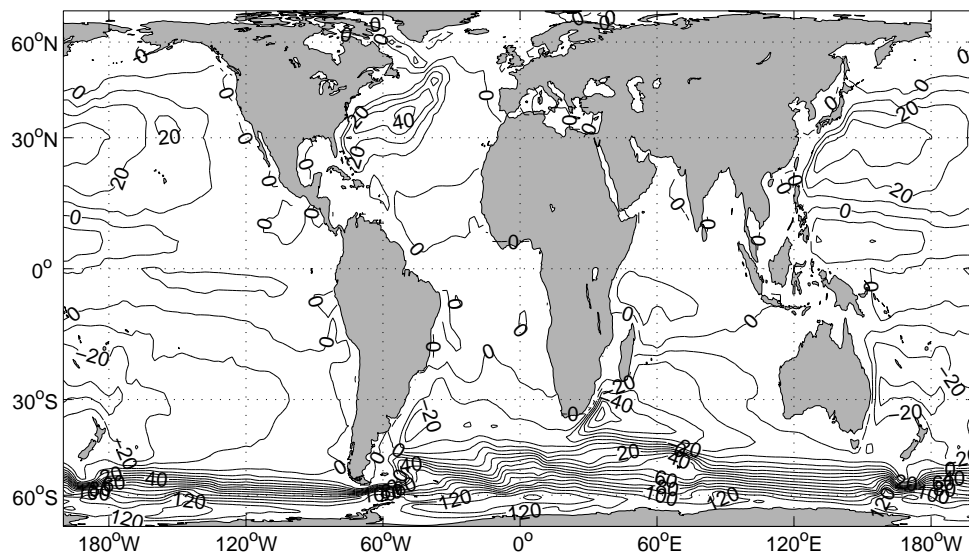**Figure 8.** Global overturning stream function in Sv. The contour interval is 2 Sv.

Figure 9. Barotropic stream function in Sv. The contour interval is 10 Sv.

year") of the Common Ocean-ice Reference Experiments (CORE) data set [*Large and Yeager*, 2004]. Wind stress and buoyancy fluxes are computed from bulk formulae [*Large and Pond*, 1981, 1982; *Large and Yeager*, 2004].

Horizontal mixing is parameterized following *Gent and McWilliams* [1990] with a variable diffusivity following *Visbeck et al.* [1996] with an imposed maximum of $600 \, \text{m}^2 \, \text{s}^{-1}$ and *Large et al.* [1997]'s slope clipping scheme; the horizontal viscosity for harmonic mixing of momentum is flow dependent according to a scheme by *Leith* [1996]. Resulting maximum viscosities are on the order of $5 \times 10^4 \, \text{m}^2 \, \text{s}^{-1}$ in western boundary currents and the Antarctic Circumpolar Current. In most parts of the ocean the viscosities are much lower. For vertical mixing, the KPP-scheme [*Large et al.*, 1994] is used. Density is computed from a fully non-linear equation of state [*McDougall et al.*, 2003]. No surface restoring to climatology is applied.

The dynamic-thermodynamic sea ice model is described in detail by Losch et al., (manuscript in preparation). It is based on the model used in *Menemenlis et al.* [2005], but involves a new discretization on a C-grid. Stress and buoyancy flux coupling to the ocean is standard.

In two experiments the model is spun-up for 100 years with full ice shelf-ocean interaction following *Hellmer and Olbers* [1989] and with an accelerated time step of 12 h for the tracer equations and 20 min for the momentum equations to reach a quasi-equilibrium at least for the upper waters. In the first case the ice shelf cavities are

kept open, in the second case the ice shelf cavities are closed and replaced by land.

4.2. General features of the circulation

The general circulation of this ocean model includes all features expected of a simulation of this resolution and degree of realism. For a summary, Figure 8 and Figure 9 show the global overturning stream function and the barotropic stream function of the reference run. With a Drake Passage transport of 116 Sv below the "canonical" value of 134 Sv [e.g., *Whitworth and Peterson*, 1985], the Antarctic Circumpolar Current is on the weak side, while the Atlantic overturning at $45°$ N of 28 Sv is stronger than generally estimated. The temperature and salinity bias is similar to that of recent global models of similar resolution [*Gnanadesikan et al.*, 2006].

Guided by our interest in the effects of the ice shelf cavities, we restrict any detailed analysis to the Southern Ocean, in particular the Weddell Sea. Here, the observed temperature and salinity structure [*Olbers et al.*, 1992; *Klatt et al.*, 2005] is mainly preserved after the spin-up, but a warm bias compared to climatology [*Levitus and Boyer*, 1994] is clearly visible in the Warm Deep Water (WDW) and bottom waters in the Weddell Sea (Weddell Sea Bottom Water, WSWB), see Figure 10. This warm bias is associated with a haline bias (not shown); these biases are not unusual for ocean models with this resolution and time scale [see e.g., *Gnanadesikan et al.*, 2006]. The warming of the WDW does not have local causes but can be explained by the inflow of overly warm Circumpolar Deep Water (CDW) into the Weddell gyre east of the Greenwich Meridian. The
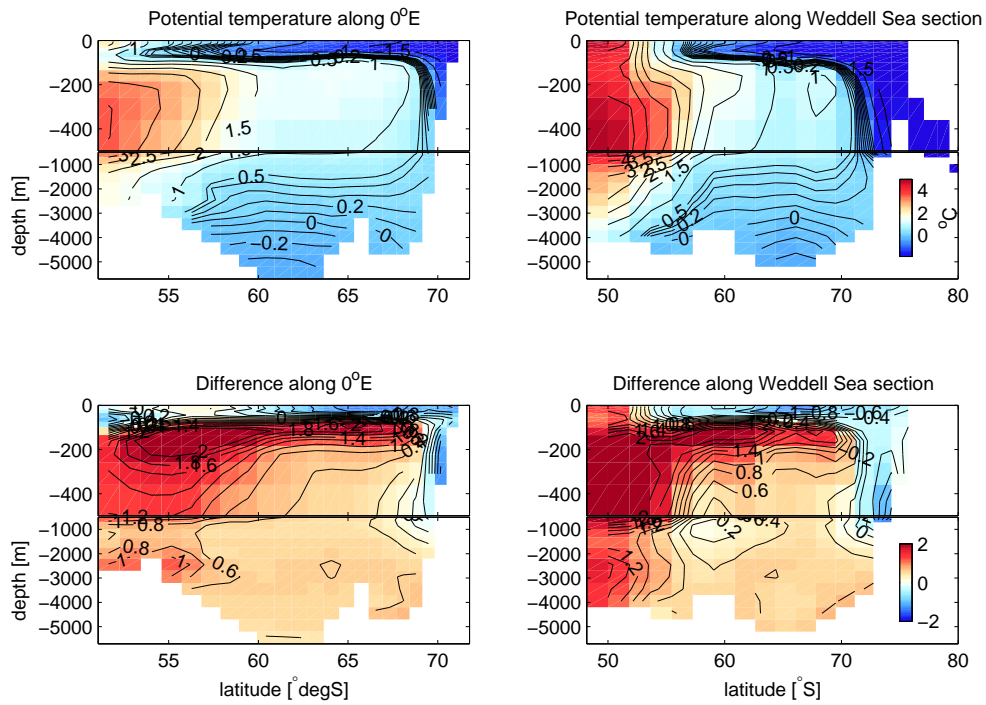
Figure 10. Top: Two selected sections of potential temperature in the Weddell Sea. Left: A one year mean of sections along the $0°$ meridian. Right: A section through the Weddell Sea from $(75°\,W, 80°\,S)$ to $(15°\,W, 50°\,S)$ [see also *Timmermann and Beckmann*, 2004]. Bottom: Difference to climatology (model minus climatology) [*Levitus and Boyer*, 1994].

bottom waters are warming because there is little to no flux of cold water down the continental slopes of the Weddell Sea, which is a typical problem of z-coordinate models without a special bottom layer treatment [e.g., *Beckmann and Doescher*, 1997; *Campin and Goosse*, 1999].

The Weddell Gyre with a mean transport of a little over $26\,\mathrm{Sv}$ is weaker than in other simulations with a σ-coordinate model [*Beckmann et al.*, 1999; *Timmermann et al.*, 2002a], but stronger than, for example, in the z-coordinate model of *Timmermann et al.* [2005].

4.3. Circulation in the Filchner-Ronne Ice Shelf cavity

The mean depth-averaged circulation in the Filchner-Ronne Ice Shelf (FRIS) cavity is shown in Figure 11. In some of the previous model results the circulation underneath the FRIS is determined largely by geostrophic contours, and hence by water column thick-
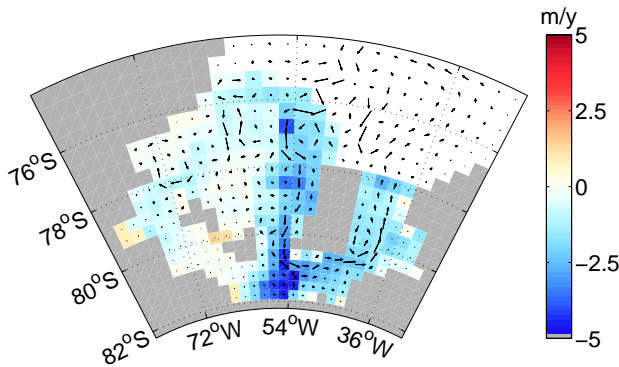

Figure 12. Vertical mean of potential temperature difference between a run with and without Filchner-Ronne and Ross Sea ice shelf cavities (ice shelf minus no ice shelf, in $°C$). The magenta line in the temperature plot marks the location of the section along the anomaly minimum in Figure 13.

Figure 11. Depth-averaged mean circulation pattern and freshwater flux into the ocean (in m/y, negative values mean melting) underneath the Filchner-Ronne Ice Shelf.
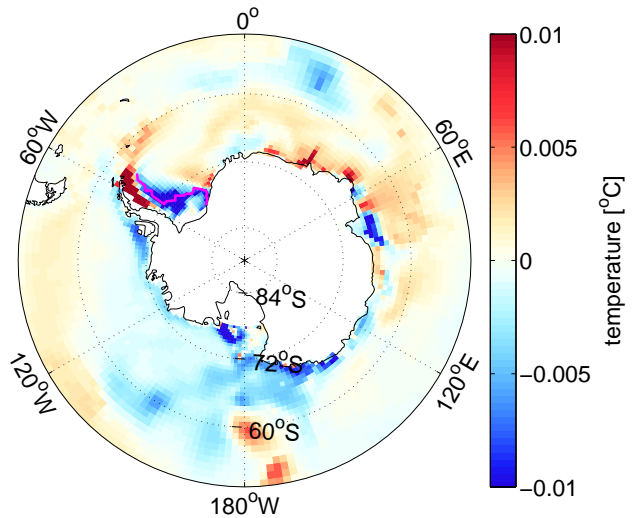
ness [*Grosfeld et al.*, 1997; *Gerdes et al.*, 1999]. The circulation in Figure 11 does not follow geostrophic contours, but it is similar to the solutions shown in *Timmermann et al.* [2002b, their 1989 solution] and *Jenkins and Holland* [2002]: The water enters in the western part of the ice shelf, circulates counter-clockwise (anti-cyclonically) around Berkner Island and leaves the cavity as cold and fresh water through the Filchner Trough in the east. As a side remark, the
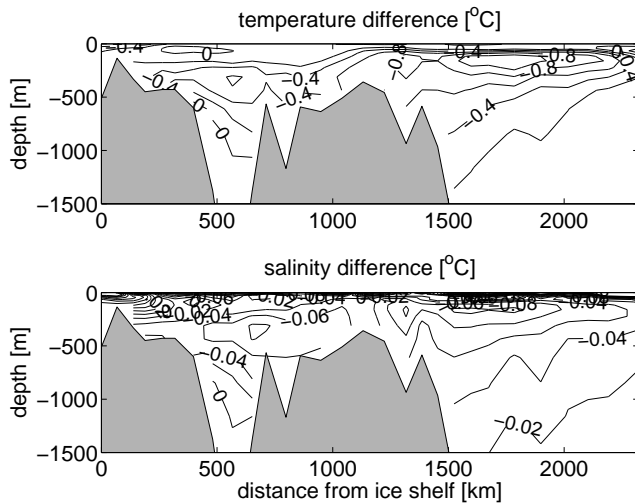
Figure 13. Vertical section of potential temperature (in °C) and salinity difference between a run with and without Filchner-Ronne and Ross Sea ice shelf cavities (ice shelf minus no ice shelf). The location of the section along the anomaly minimum is shown in the temperature plot of Figure 12.
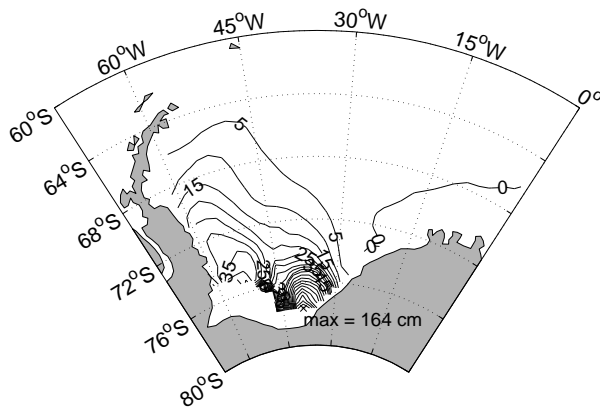

Figure 14. Difference of sea ice volume per unit area in the Weddell Sea between a run with and without ice shelf cavities (ice shelf minus no ice shelf, in centimeters).

orientation of the flow is sensitive to the circulation in the Weddell Sea: In more viscous runs (with a constant viscosity coefficient of $5 \times 10^4 \, \text{m}^2 \, \text{s}^{-1}$), the direction of the circulation reverses to cyclonic and cold and fresh water leaves the cavity in the West, similar to *Timmermann et al.* [2002b]'s 1992 solution (not shown). With *Hellmer and Olbers* [1989]'s standard parameters for the ice shelf ocean interaction (in particular the constant exchange coefficients for heat and fresh water of $1 \times 10^{-4} \, \text{m} \, \text{s}^{-1}$ and $5.05 \times 10^{-7} \, \text{m} \, \text{s}^{-1}$, respectively), the mean melt rate underneath FRIS is $0.94 \, \text{m} \, \text{y}^{-1}$, maximum melt and freezing rates can be as high as $7.8 \, \text{m} \, \text{y}^{-1}$ and $1.4 \, \text{m} \, \text{y}^{-1}$, respectively. Melt rates are highest near the grounding line where the ice shelf is deepest (Figure 11). The implied mean total freshwater flux is $13.9 \times 10^3 \, \text{m}^3 \, \text{s}^{-1}$, hence three to four times higher than in previous studies [*Hellmer*, 2004; *Timmermann et al.*, 2001]. There are multiple possible reasons for this overestimation. First, the current implementation with constant exchange coefficients may be inappropriate. Velocity dependent exchange coefficients following *Holland and Jenkins* [1999], diagnosed for

the solution in Figure 11, yield mean values that are only 20% of those of *Hellmer and Olbers* [1989]. In a sensitivity experiment with such values, the mean freshwater flux for FRIS can be reduced by over 50% without changing the circulation and melting pattern significantly (not shown). Second, poor vertical resolution may be a problem. The vertical z-layer thickness in the ice shelf cavity is on the order of 100 to 400 m (the actual cell thickness can be smaller due to the partial cell treatment of the topography), so that cold and fresh melt water at the ice-ocean interface is immediately mixed into a large volume and the temperature at the ice shelf interface remains well above freezing, leading to more melting. Third, as a consequence of a bias of the model far away from the ice shelves, the water entering the ice shelves may be too warm (see Figure 10). Then, ice shelf processes can not cool the water sufficiently, which may also explain the absence of a large region of refreezing west of Berkner Island that is observed in previous simulations [*Gerdes et al.*, 1999; *Jenkins and Holland*, 2002]. In the present simulation this region is characterized by reduced melt rates but no refreezing.

4.4. Effect of ice shelf cavities on the global circulation

Figure 12 shows the vertically averaged temperature difference between a run with and without ice shelf cavities. In the Weddell Sea, warm and saline water enters the FRIS in the west and emerges
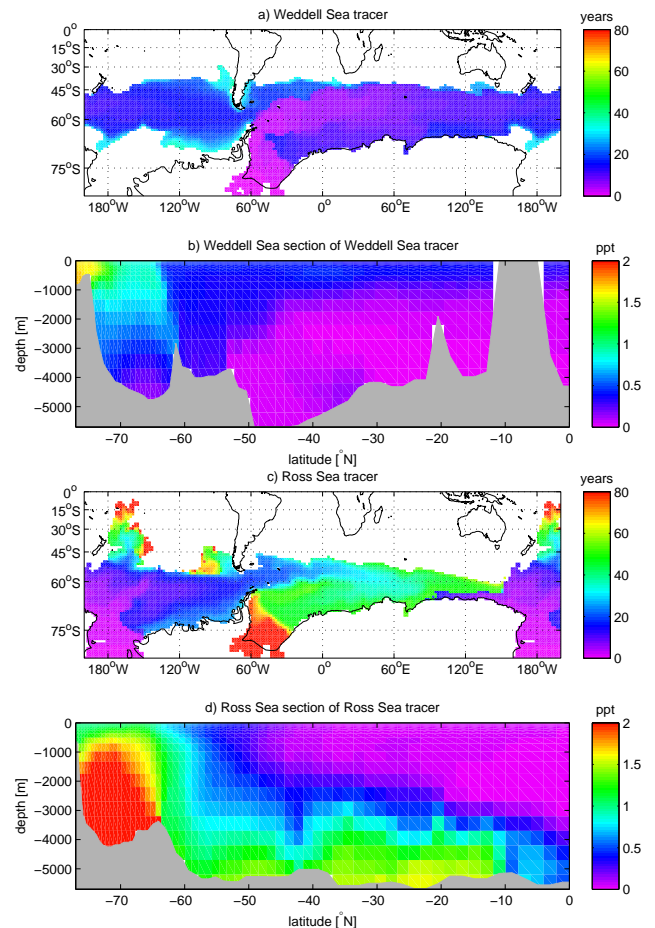

Figure 15. Arrival time (in years) of a threshold concentration of 1 ppt anywhere in the water column for a passive dye tracer that is released in a) the Filchner-Ronne Ice Shelf cavity, c) the Ross Sea Ice Shelf cavity. The vertical distribution of the corresponding tracers (in ppt of the original concentration) after 100 years are averaged over longitude bands of b) $36°$ W to $56°$ W and d) $160°$ E to $160°$ W.

from the Filchner Trough as cold and fresh water east of Berkner Island (Figure 11). The water is buoyant and rises to a lower depth (parameterized by vertical mixing of the KPP scheme). The cold and fresh anomaly moves off the shelf and enters the circulation system of the Weddell Gyre and rises further until it reaches the surface east of the northern tip of the Antarctic peninsula (Figures 12 and 13). Part of the cold and fresh water reaches depths of approximately 1500 m after leaving the shelf (Figure 13), but deep waters below the exit depth of the Filchner Trough tend to be warmer than in the run without ice shelf cavities pointing to less bottom water formation as discussed in *Hellmer* [2004]. The inclusion of the ice shelf processes also lead to more sea ice with a pattern (Figure 14) that is comparable to that found by *Hellmer* [2004]. Furthermore, in the run with ice shelves the northward circulation along the Antarctic peninsula is moved off the shelf, allowing a warm anomaly on the shelf. The origin of this anomaly, which is compensated by a negative salinity anomaly, is not clear.

Passive tracer simulations, in which the ice shelf cavities are filled once with passive tracers of concentration 1 at the beginning of the integration, illustrate that in the Ross Sea, the cold and fresh glacial melt spreads westwards in the Antarctic coastal current (Figure 15c). Also the water mass modified by melt water tends to be less buoyant than surrounding waters and sinks to greater depths where it spreads northwards across the equator (visible as a northward pointing tongue along approximately 170° W in Figure 15c and d). The glacial melt water from the Weddell Sea circulates along the shelf break. Along its path it is diluted and cannot sink as deep as in the Ross Sea although small tracer concentrations are found below 2000 m. Thus, the melt water from the FRIS is confined to the Antarctic Circumpolar Current (Figure 15a and b); it circulates around Antarctica before re-entering the South Atlantic through the Drake Passage along the cold water path [*Rintoul*, 1991].

The potential influence of ice-shelf melt water on the global circulation was the initial driving force for this work, but the simulation presented here is too short to provide conclusive evidence about inter-hemispheric or global effects. However, it is observed that the inclusion of ice shelf cavities has an effect particularly in the sensitive convection areas in the North Atlantic (not shown). A similar effect was observed by *Hellmer et al.* [2005] who introduced the effect of ice shelf cavities by assimilating data from a regional model with ice shelves into a global model. The observation in the present model run should be taken with caution because of the solid boundary at 80° N in this simulation, although at this point it may be speculated that the anomalies represent small changes in the general circulation, for example a horizontal shift of convection events. These changes may be triggered by baroclinic anomaly waves originating in the Southern Ocean. How and on what time scales these shifts occur is beyond the scope of this paper and will be discussed elsewhere.

5. Conclusions

We implemented an ice shelf cavity model in a z-coordinate ocean model. Difficulties associated with spurious horizontal mixing in z-coordinate models can be overcome by sufficient grid resolution and parameterized isopycnic mixing. While not essential, the partial cell treatment of topography makes it possible to represent the complicated topography of the ice shelves more accurately. The new model approach compares favorably with established ice shelf models in the framework of ISOMIP. The pressure gradient error which is notorious in terrain following models, is not an issue for z-coordinate models by construction. This can be shown in a second ISOMIP experiment where the thermodynamic ice-ocean interaction is turned off; as expected, the model remains at rest within the 64bit working precision.

Solid (castellated) boundaries and the Coriolis term are a perpetual source of noise on a C-grid. Furthermore, if the vertical resolution is not sufficient to resolve the ice shelf topography, the effect of castellated boundaries is amplified at the ice-ocean interface because there, as opposed to lateral or bottom boundaries, the effect of the local thermodynamic ice-ocean interaction is a function of varying cell thickness. In principle, the noise emerging from the thermodynamics can be reduced by introducing a simple boundary layer scheme, but both types of noise are damped effectively with general techniques such as bi-harmonic viscosity (not shown) and a special treatment of the Coriolis term [*Adcroft et al.*, 1997]. In a realistic global ocean simulation this noise is not observed.

In practice, one has to find a compromise between affordable resolution in a global model and the necessary resolution beneath ice shelves. For the ISOMIP experiment, the ice shelf slope is reasonably resolved with a vertical layer thickness of 100 m and less: The vertical resolution dependence of mean melt rates and internal mixing becomes small in experiments with a vertical resolution better than 100 m. The prescribed large ISOMIP mixing parameters emphasize the z-coordinate models' weakness of spurious diapycnic mixing. Although the experiments with horizontal mixing can reproduce the rising light melt water plumes, spurious diapycnal mixing can be reduced dramatically with the help of an isopycnic mixing scheme [*Gent and McWilliams*, 1990] and high-order advection schemes, thus leading to a thinner boundary layer along the ice shelf.

In a numerical experiment simulating the global ocean the principal pattern of the circulation in the FRIS is reproduced. Estimated melt rates are higher than the observed and previously simulated values. This can be explained by the fact that the vertical resolution in the depth range of the ice shelf cavities is poor and more melting is required to cool a large (grid cell) volume of water. Previous models with terrain-following or isopycnic vertical coordinates have the advantage of high vertical resolution (in shallow cavities the vertical resolution in σ-models can be so high that it imposes constraints on the numerical stability, H. Hellmer, personal communication), and can resolve thin layers of cold water beneath the ice shelf. As a possible solution for z-coordinate models, the exchange coefficients for heat and fresh water could be made a function of the local cell thickness or interior mixing (as provided by the oceanic mixing scheme) in order to reduce the melt rates. Further, parameterizing the exchange coefficient as a function of friction velocity following *Holland and Jenkins* [1999] could improve the melt rate estimates in a global context. One can also speculate that the melt rate is controlled to a large extent by the properties of the water entering the ice shelf cavities. This water is too warm in the present simulation leading to too strong melting.

The approach presented here can be implemented in any z-coordinate model that supports partial cells in the vertical. Because of the numerical effects and the limited resolution near the ice-ocean interface in z-models it may be desirable to combine the benefits of a z-coordinate model (no pressure gradient error over topography) with the high resolution at the ice-ocean interface of the terrain-following coordinate model of, for example, *Beckmann et al.* [1999]. This can be achieved with the help of a surface following coordinate system [*Adcroft and Campin*, 2004]. Alternatively, a boundary layer model analogous to bottom boundary layer models [e.g., *Killworth and Edwards*, 1999] could be implemented. However, for both approaches, the pressure gradient errors need to be addressed in the same way as in terrain-following coordinate models.

In the coarse global ocean simulation of this study, the cold and fresh melt water from the ice shelf cavities leads to additional sea ice thickness. This points to a reduced production of bottom water and thus a reduced overturning in the model [*Hellmer*, 2004]. The glacial melt of the Ross Sea ice shelf cavity can be traced along the bottom as far north as 15° S on a 100 year timescale implying far field effects of ice shelf processes. In contrast, glacial melt from the Weddell Sea is confined to the ACC. Previous circulation models with ice-shelf cavities were regional models and could not detect these large scale effects. Both local, regional and global effects emphasize that for ocean state predictions, the (effects of) ice shelf-ocean interaction ought to be included in ocean general circulation models.

Appendix A: Thermodynamics

Two different thermodynamic schemes are used in this paper. For the ISOMIP experiments in Section 3, the upward heat flux Q at the interface is parameterized in a bulk formulation proportional to the temperature difference between the ice shelf base and the sea-water

$$Q = \rho c_p \gamma_T (T_W - T_b) \quad \text{(A1)}$$

where ρ is the density of sea-water, $c_p = 3974\,\mathrm{J\,kg^{-1}\,K^{-1}}$ is the specific heat capacity of water, and $\gamma_T = 10^{-4}\,\mathrm{m\,s^{-1}}$ the turbulent exchange coefficient. T_W is the temperature of the model cell adjacent to the ice-water interface. The temperature at the interface T_b is assumed to be the in-situ freezing point of sea-water T_f which is computed from

$$T_f = 1.710523 \times 10^{-3}\, S_W^{3/2} - 2.154996 \times 10^{-4}\, S_W^2$$
$$- 0.0575\, S_W - 7.53 \times 10^{-4}\, p_W \quad \text{(A2)}$$

with the salinity S_W and the pressure p_W (in dBar) in the cell at the ice-water interface [*Gill*, 1982].

Neglecting the heat flux through the ice, all heat is used for basal melting and freezing. The associated upward freshwater flux (negative melt rate, in units of fresh water mass per time) can be computed by

$$q = -\frac{Q}{L} \quad \text{(A3)}$$

with the latent heat of fusion $L = 334000\,\mathrm{J\,kg^{-1}}$. Upward heat flux implies basal melting therefore a downward freshwater flux, hence the minus sign. From the freshwater flux a virtual salt flux is computed using a constant reference salinity of 34.4 according to the ISOMIP specifications.

The more realistic three-equation-thermodynamics of *Hellmer and Olbers* [1989] with modifications following *Jenkins et al.* [2001] is sketched for completeness. Instead of Eq. (A3) the total heat flux in Eq. (A1) is expressed as

$$Q = c_p(\rho\gamma_T - q)(T_W - T_b) = -Lq - \rho_I c_{p,I} \kappa \frac{(T_S - T_b)}{h} \quad \text{(A4)}$$

where $\rho_I = 920\,\mathrm{kg\,m^{-3}}$, $c_{p,I} = 2000\,\mathrm{J\,kg^{-1}\,K^{-1}}$, and T_S are the density, heat capacity and the surface temperature of the ice shelf; $\kappa = 1.54 \times 10^{-6}\,\mathrm{m^2\,s^{-1}}$ is the heat diffusivity through the ice-shelf and h is the ice-shelf draft. The second term on the right hand side describes the heat flux through the ice shelf. A constant surface temperature $T_S = -20\,^\circ\mathrm{C}$ is imposed. From the salt budget, the (virtual) salt flux across the shelf ice-ocean interface is equal to the (virtual) salt flux due to melting and freezing:

$$(\rho\gamma_S - q)(S_W - S_b) = -S_b q, \quad \text{(A5)}$$

where $\gamma_S = 5.05 \times 10^{-3}\gamma_T$ is the turbulent salinity exchange coefficient, and S_W and S_b are defined in analogy to temperature as the salinity of the model cell adjacent to the ice-water interface and at the interface, respectively. Equations (A4) and (A5), together with a linear equation for the freezing temperature of sea water can be solved for S_b or T_b, from which the freshwater flux q and the heat flux Q can be computed. This formulation yields smaller melt rates than the simpler formulation of equations (A1) to (A3) because the freshwater flux due to melting decreases the salinity which raises the freezing point temperature and thus leads to less melting at the interface.

References

Adcroft, A., and J.-M. Campin (2004), Rescaled height coordinates for accurate representation of free-surface flows in ocean circulation models, *Ocean Modelling*, 7(3-4), 269–284.

Adcroft, A., C. Hill, and J. Marshall (1997), Representation of topography by shaved cells in a height coordinate ocean model, *Mon. Wea. Rev.*, 125(9), 2293–2315.

Adcroft, A., C. Hill, and J. Marshall (1999), A new treatment of the Coriolis terms in C-grid models at both high and low resolutions, *Mon. Wea. Rev.*, 127, 1928–1936.

Beckmann, A., and R. Doescher (1997), A method for improved representation of dense water spreading over topography in geopotential-coordinate models, *J. Phys. Oceanogr.*, 27, 581–591.

Beckmann, A., and H. Goosse (2003), A parameterization of ice shelf-ocean interaction for climate models, *Ocean Modelling*, 5(2), 157–170.

Beckmann, A., H. H. Hellmer, and R. Timmermann (1999), A numerical model of the Weddell Sea: Large-scale circulation and water mass distribution, *J. Geophys. Res.*, 104(C10), 23,375–23,392.

Bleck, R. (2002), An oceanic general circulation model framed in hybrid isopycnic-cartesian coordinates, *Ocean Modelling*, 4, 55–88.

British Oceanographic Data Center (2003), Centenary edition of the GEBCO digital atlas [CD-ROM], Liverpool, UK: Published on behalf of the Intergovernmental Oceanographic Commission and the International Hydrographic Organization.

Campin, J.-M., and H. Goosse (1999), Parameterization of density-driven downsloping flow for a coarse-resolution ocean model in z-coordinate, *Tellus*, 51A(412-430).

Daru, H., and C. Tenaud (2004), High order one-step monotonicity-preserving schemes for unsteady compressible flow calculations, *J. Comp. Phys.*, 193, 563–594.

Dewar, W. K., Y. Hsueh, T. J. McDougall, and D. Yuan (1998), Calculation of pressure in ocean simulations, *J. Phys. Oceanogr.*, 28(4), 577–588.

Foldvik, A., T. Gammelsrød, and T. Tørresen (1985), Circulation and water masses on the southern Weddell Sea shelf, in *Oceanology of the Antarctic Continental Shelf*, edited by S. S. Jacobs, Antarc. Res. Ser., pp. 5–20, AGU, Washington, D.C.

Fox, A. J., and A. P. R. Cooper (1994), Measured properties of the Antarctic ice sheet derived from the SCAR Antarctic digital database, *Polar Rec.*, 30, 201–206.

Gent, P. R., and J. C. McWilliams (1990), Isopycnal mixing in ocean circulation models, *J. Phys. Oceanogr.*, 20(1), 150–155.

Gerdes, R., J. Determann, and K. Grosfeld (1999), Ocean circulation beneath Filchner-Ronne Ice Shelf from three-dimensional model results, *J. Geophys. Res.*, 104(C7), 15,827–15,842.

Gill, A. E. (1982), *Atmosphere-Ocean Dynamics*, *International Geophysics Series*, vol. 30, 666 pp., Academic Press, San Diego, CA.

Gnanadesikan, A., et al. (2006), GFDL's CM2 global coupled climate models. Part II: The baseline ocean simulation, *J. Climate*, 19(3), 675–697.

Grosfeld, K., R. Gerdes, and J. Determann (1997), Thermohaline circulation and interaction between ice shelf cavities and the adjacent open water, *J. Geophys. Res.*, 102(C7), 15,595–15,610.

Hellmer, H. H. (2004), Impact of Antarctic ice shelf melting on sea ice and deep ocean properties, *Geophys. Res. Lett.*, 31(10), L10,307, doi: 10.1029/2004GL019506.

Hellmer, H. H., and D. J. Olbers (1989), A two-dimensional model of the thermohaline circulation under an ice shelf, *Antarct. Sci.*, 1, 325–336.

Hellmer, H. H., M. P. Schodlok, M. Wenzel, and J. G. Schröter (2005), On the influence of adequate Weddell Sea characteristics in a large-scale global ocean circulation model, *Ocean Dynamics*, 55(2), 88–99, doi: 10.1007/s10236-005-0112-4.

Holland, D. M., and A. Jenkins (1999), Modeling thermodynamic ice-ocean interactions at the base of an ice shelf, *J. Phys. Oceanogr.*, 29(8), 1787–1800.

Holland, D. M., and A. Jenkins (2001), Adaptation of an isopycnic coordinate ocean model for the study of circulation beneath ice shelves, *Mon. Wea. Rev.*, 129, 1905–1927.

Holland, D. M., et al. (2003), The ice shelf - ocean model intercomparison project (ISOMIP), *AGU Fall Meeting Abstracts*, pp. A5+.

Hunter, J., M. Hemer, and M. Craven (2004), Modelling the circulation under the Amery Ice Shelf, in *Forum for Research into Ice Shelf Processes (FRISP)*, *FRISP Report*, vol. 15, edited by L. H. Smedsrud, pp. 67–72, Bjerknes Centre for Climate Research, Bergen, Norway.

Hunter, J. R. (2006), Specification for test models of ice shelf cavities, *Tech. rep.*, Antarctic Climate and Ecosystems Cooperative Research Centre, Hobart, Australia (http://staff.acecrc.org.au/~johunter/isomip/test_cavities.pdf).

Jackett, D. R., and T. J. McDougall (1995), Minimal adjustment of hydrographic profiles to achieve static stability, *J. Atmos. Oceanic Technol.*, 12(4), 381–389.

Jenkins, A., and D. M. Holland (2002), A model study of ocean circulation beneath Filchner-Ronne ice shelf, Antarctica: Implications for bottom water formation, *Geophys. Res. Lett.*, 29(8), 1193, doi: 10.1029/2001GL014589.

Jenkins, A., H. H. Hellmer, and D. M. Holland (2001), The role of meltwater advection in the formulation of conservative boundary conditions at an ice-ocean interface, *J. Phys. Oceanogr.*, *31*, 285–296.

Killworth, P. D., and N. R. Edwards (1999), A turbulent bottom boundary layer code for use in numerical ocean models, *J. Phys. Oceanogr.*, *29*(6), 1221–1238.

Klatt, O., E. Fahrbach, M. Hoppeman, and G. Rohardt (2005), The transport of the Weddell Gyre across the Prime Meridian, *Deep-Sea Res. II*, *52*, 513–528.

Large, W. G., and S. Pond (1981), Open ocean momentum flux measurements in moderate to strong winds, *J. Phys. Oceanogr.*, *11*, 324–336.

Large, W. G., and S. Pond (1982), Sensible and latent heat flux measurements over the ocean, *J. Phys. Oceanogr.*, *12*, 464–482.

Large, W. G., and S. Yeager (2004), Diurnal to decadal global forcing for ocean and sea-ice models: the data sets and flux climatologies, *Tech. Rep. NCAR/TN-460+STR*, CGD Division of the National Center for Atmospheric Research, Boulder, CO.

Large, W. G., J. C. McWilliams, and S. C. Doney (1994), Oceanic vertical mixing: A review and a model with a nonlocal boundary layer parameterization, *Rev. Geophys.*, *32*(4), 363–404.

Large, W. G., G. Danabasoglu, S. C. Doney, and J. C. McWilliams (1997), Sensitivity of surface forcing and boundary layer mixing in a global ocean model: Annual-mean climatology, *J. Phys. Oceanogr.*, *27*(11), 2418–2447.

Legg, S., R. W. Hallberg, and J. B. Girton (2006), Comparison of entrainment in overflows simulated by *z*-coordinate, isopycnal and nonhydrostatic models, *Ocean Modelling*, *11*(1–2), 69–97.

Leith, C. E. (1996), Stochastic models of chaotic systems, *Physica D*, *98*, 481–491.

Levitus, S., and T. Boyer (1994), World Ocean Atlas 1994. Volume 4: Temperature, *NOAA Atlas NEDSIS 4*, NOAA, Washington D.C.

Levitus, S., R. Burgett, and T. Boyer (1994), World Ocean Atlas 1994. Volume 3: Salinity, *NOAA Atlas NEDSIS 3*, NOAA, Washington D.C.

Lewis, E. L., and R. G. Perkins (1986), Ice pumps and their rates, *J. Geophys. Res.*, *91*(C10), 11,756–11,762.

Losch, M., A. Adcroft, and J.-M. Campin (2004), How sensitive are coarse general circulation models to fundamental approximations in the equations of motion?, *J. Phys. Oceanogr.*, *34*(1), 306–319.

Marks, K. M., and W. H. F. Smith (2006), An evaluation of publicly available global bathymetry grids, *Marine Geophysical Researches*, *27*(1), 19–34, doi:10.1007/s11001-005-2095-4.

Marshall, J., A. Adcroft, C. Hill, L. Perelman, and C. Heisey (1997), A finite-volume, incompressible Navier Stokes model for studies of the ocean on parallel computers, *J. Geophys. Res.*, *102*(C3), 5753–5766.

Marshall, J., A. Adcroft, J.-M. Campin, C. Hill, and A. White (2004), Atmosphere-ocean modeling exploiting fluid isomorphisms, *Mon. Wea. Rev.*, *132*(12), 2882–2994.

McDougall, T. J., D. R. Jackett, D. G. Wright, and R. Feistel (2003), Accurate and computationally efficient algorithms for potential temperature and density of seawater, *J. Atmos. Oceanic Technol.*, *20*(5), 730–741.

Menemenlis, D., et al. (2005), NASA supercomputer improves prospects for ocean climate research, *Eos Trans. AGU*, *86*(9), 89, 95–96.

Millero, F. J. (1978), Annex 6, freezing point of seawater, *Unesco Techn. Papers in Marine Science 28*, UNESCO, Paris.

MITgcm Group (2002), MITgcm Release 1 Manual, *Online documentation*, MIT/EAPS, Cambridge, MA 02139, USA, http://mitgcm.org/sealion/online_documents/manual.html.

Olbers, D., V. Gouretski, G. Seiss, and J. Schröter (1992), *Hydrographic Atlas of the Southern Ocean*, 99 pp., Alfred-Wegener-Institut für Polar- und Meeresforschung, Bremerhaven, Germany.

Rintoul, S. R. (1991), South Atlantic interbasin exchange, *J. Geophys. Res.*, *96*(C2), 2675–2692.

Schodlok, M. P., J. G. S. Manfred Wenzel, and H. H. Hellmer (2007), Regional and global effects of Southern Ocean constraints in a global model, *submitted to Ocean Dynamics*.

Smith, W. H. F., and D. T. Sandwell (1997), Global seafloor topography from satellite altimetry and ship depth soundings, *Science*, *277*, 1957–1962.

Thoma, M., K. Grosfeld, and M. A. Lange (2006), Impact of the Eastern Weddell Ice Shelves on water masses in the eastern Weddell Sea, *J. Geophys. Res.*, *111*(C12), C12,010, doi:10.1029/2005JC003212.

Timmermann, R., and A. Beckmann (2004), Parameterization of vertical mixing in the Weddell Sea, *Ocean Modelling*, *6*(1), 83–100.

Timmermann, R., A. Beckmann, and H. Hellmer (2001), The role of sea ice in the fresh water budget of the Weddell Sea, *Ann. Glaciol.*, *33*, 419–424.

Timmermann, R., A. Beckmann, and H. H. Hellmer (2002a), Simulation of ice-ocean dynamics in the Weddell Sea. Part I: Model configuration and validation, *J. Geophys. Res.*, *107*(C3), 3024, doi:10.1029/2000JC000741.

Timmermann, R., H. H. Hellmer, and A. Beckmann (2002b), Simulations of ice-ocean dynamics in the Weddell Sea. Part II: Interannual variability 1985 - 1993, *J. Geophys. Res.*, *107*(C3), 3025, doi:10.1029/2000JC000742.

Timmermann, R., H. Goosse, G. Madec, T. Fichefet, C. Ethe, and V. Duliere (2005), On the representation of high latitude processes in the ORCA-LIM global coupled sea ice-ocean model, *Ocean Modelling*, *8*(1–2), 175–201, doi:10.1016/j.ocemod.2003.12.009.

Visbeck, M., J. Marshall, and H. Jones (1996), Dynamics of isolated convective regions in the ocean, *J. Phys. Oceanogr.*, *26*(9), 1721–1734.

Whitworth, T., III, and R. G. Peterson (1985), Volume transport of the Antarctic Circumpolar Current from bottom pressure measurements, *J. Phys. Oceanogr.*, *15*(6), 810–816.

M. Losch, Alfred-Wegener-Institut für Polar- und Meeresforschung Postfach 120161, 27515 Bremerhaven, Germany. (Martin.Losch@awi.de)